

Multimodal Abnormity-Aware Model for Ocular Disease Diagnosis

Siqi Pan

Abstract

We devise a novel model, the Multimodal Abnormity-Aware Model (MAAM), for assisting ocular disease diagnosis. The MAAM enables input of 2 kinds of ophthalmological images, namely optical coherence tomography (OCT) and color fundus images, and simulates the decision-making process by deducing the disease from abnormities. The model is composed of 2 submodels, the Abnormity Models and the Diagnosis Model, where the Abnormity Models identify 11 OCT abnormities and 8 fundus abnormities, and the Diagnosis Model identifies 12 diseases by integrating features from the former model. In MAAM, we introduce the fusion mechanism, the concept of codominant abnormities and diseases, and the Abnormity-to-Disease Criteria. The model breaks the black box of complex neural network and expose more interpretable information for the reference of ophthalmologists. And it gets the overall accuracy of 89% and thus the feasibility is verified.

1 Background

Ocular diseases can be diagnosed through various methods, including using optical coherence tomography (OCT) and color fundus images. Ophthalmologists usually identify ocular abnormalities to deduce the disease. Traditionally, the diagnosis primarily depends on the professional experience and knowledge of the ophthalmologists, which may result in high misdiagnosis rate and under-utilization of medical data. With the widespread application of artificial intelligence (AI), deep learning (DL) has made great contributions in providing support to patients in remote areas by sharing expert knowledge [5]. By leveraging DL, researchers have developed auxiliary diagnosis programs to help ophthalmologists in the process. Many studies use convolutional neural networks (CNN) to analyze ocular images.

Some commonly used CNNs are VGG, ResNet, and Inception [8]. And for segmenting images and finding abnormalities, U-net is widely used [23]. With regards to training CNNs, most studies use transferred learning, which consists of three steps: learning, fine-tuning, and validation.

Some studies directly predict the disease from OCT images. Li, Chen, Liu, *et al.* (2019) used ResNet to analyze OCT images and distinguish between choroidal neovascularization (CNV), diabetic macular edema (DME), drusen, and healthy eyes. In addition, they performed occlusion testing to find out the regions that are the most important in diagnosis [18]. Yoo, Choi, and Kim (2021) used generative adversarial network (GAN) and Inception-v3 together with a few-shot dataset to investigate the feasibility of improving OCT diagnosis of rare ocular diseases [30]. They handled

the issues of training image shortage and data imbalance by creating ocular disease OCT images from healthy OCT images. Kermany, Goldbaum, Cai, *et al.* (2018) conducts medical diagnosis and identifies treatable diseases by image-based deep learning. They also provided a widely used database including more than one hundred thousand OCT labeled images for 3 diseases [14].

Some other studies can identify ocular abnormalities from annotated OCT images. Camino, Wang, Wang, *et al.* (2018) used DL to identify the region of preserved photoreceptors on *en face* OCT in choroideremia and retinitis pigmentosa (RP) [6]. Srinivasan, Kim, Mettu, *et al.* (2014) detected DME and dry age-related macular degeneration (dry AMD) from OCT images by flattening the image and using support vector machine (SVM) to extract the thickness information of the retinal layers [27]. Leandro, Lorenzo, Aleksandar, *et al.* (2023) implemented VGG to identify up to 8 kinds of key abnormalities and hence detect multiple diseases by using central fovea cross-section OCT [16]. Fang, Wang, Li, *et al.* (2019) developed a novel lesion-aware CNN, called LACNN, to simulate the ophthalmologists' diagnosis that focuses on ocular abnormalities. The LACNN is a U-net-like CNN which incorporates VGG16 as the baseline, and the result is impressive [9].

Other studies use fundus images to predict ocular diseases. Masumoto, Tabuchi, Nakakura, *et al.* (2019) trained deep CNN with ultrawide-field fundus images to make the CNN capable of diagnosing RP [21]. Chen, Lim, Wang, *et al.* (2021) uses color fundus photographs and multiple types of CNN (Inception V3, Inception Resnet V2, and Xception) to develop a method of early detection of RP [7]. Li, Chen, Zhang, *et al.* (2022) uses CNN to detect up to 12 fundus diseases based on colour fundus photography [17]. Son, Shin, Kong, *et al.*

(2023) presented a novel architectural and algorithmic design to comprehensively identify 15 abnormalities and diagnose 8 major ocular diseases from macula-centered fundus images. They defined a notion of counterfactual attribution ratio (CAR) to interpret the system's diagnostic reason and disclose the relationship between abnormalities and diseases [26].

In recent years, more and more DL systems began to use multi-modal information to predict ocular diseases. For automated detection system, retrieving features from both OCT images and fundus images can effectively keep the diagnosis away from bias and incompleteness. It is not always necessary to yield a better automated diagnosis result, but it does help ophthalmologist to make more accurate and holistic clinical decisions. For instance, Liu, Ling, Hahn, *et al.* (2023) combined OCT and fundus images to evaluate visual impairment in RP in terms of best-corrected visual acuity(BCVA) [19]. Xu, Wang, Yang, *et al.* (2021) leveraged a bi-modal CNN to diagnose AMD and polypoidal choroidal vasculopathy (PCV), where the architecture uses fundus and OCT images as input for transferred learning CNN and concatenates the retrieved features to classify 3 diseases including dry AMD, wet AMD and PCV [29]. And Andrearczyk2018 ingeniously combined medical images and biomedical textual information to discriminate different diseases, which is a novel method for the usage of multi-modal application [4].

The key technical problem of multi-modal diagnosis is how to fuse the results from multifarious sources. There are three types of fusion, namely early, late, and hybrid fusion. Deciding on the optimal type of fusion is part of the exploratory process in the application of DL methods [5].

2 Overview

We develop the Multimodal Abnormity-Aware Model (MAAM) to aid ophthalmologists in diagnosing ocular diseases. It considers both OCT and color fundus image inputs. In addition, it simulates the decision-making process of ophthalmologists when they examine patients, namely, first identifying the abnormalities, and then deducing the disease. The model is designed in a way that partly opens up the “black box” of DL and presents more interpretable information to ophthalmologists for the reference.

The structure of the MAAM is shown in Fig. 1.

It consists of 2 submodels: the Abnormity Model and the Diagnosis Model. We input multiple OCT and fundus images to the Abnormity Models, and output the classification of abnormalities as an input to the Diagnosis Model, which yields disease probabilities as the final result.

The Abnormity Models are de facto classifiers for abnormalities, which are symptoms that can be directly observed in the images. The MAAM identifies 11 OCT abnormalities and 8 Fundus abnormalities, as shown in Fig. 2 and Fig. 3. The abbreviations and detail information of abnormalities and diseases are tabulated in “Appendix”.

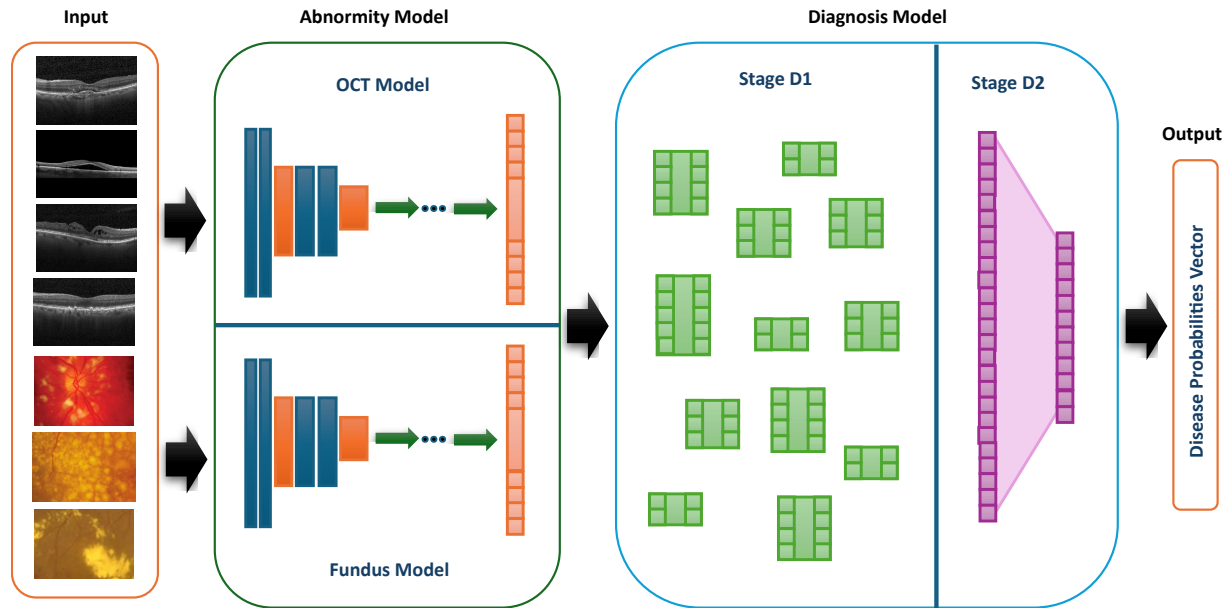


Fig. 1 Model overview

The Abnormity Models also contain 2 submodels: the OCT Model and the Fundus Model, which classify OCT and fundus abnormalities, respectively. Both of the submodels leverage CNNs with modified final fully-connected (FC) layers. We compare the performances of 4 commonly used

CNNs, ResNet152, ResNet50, ResNet18 [12] and VGG16 [25], and choose the best one for each submodel. The final FC layer in each CNN is modified so that the size of its output vector is equal to the number of OCT or fundus abnormalities. In order to normalize the output vector, we perform

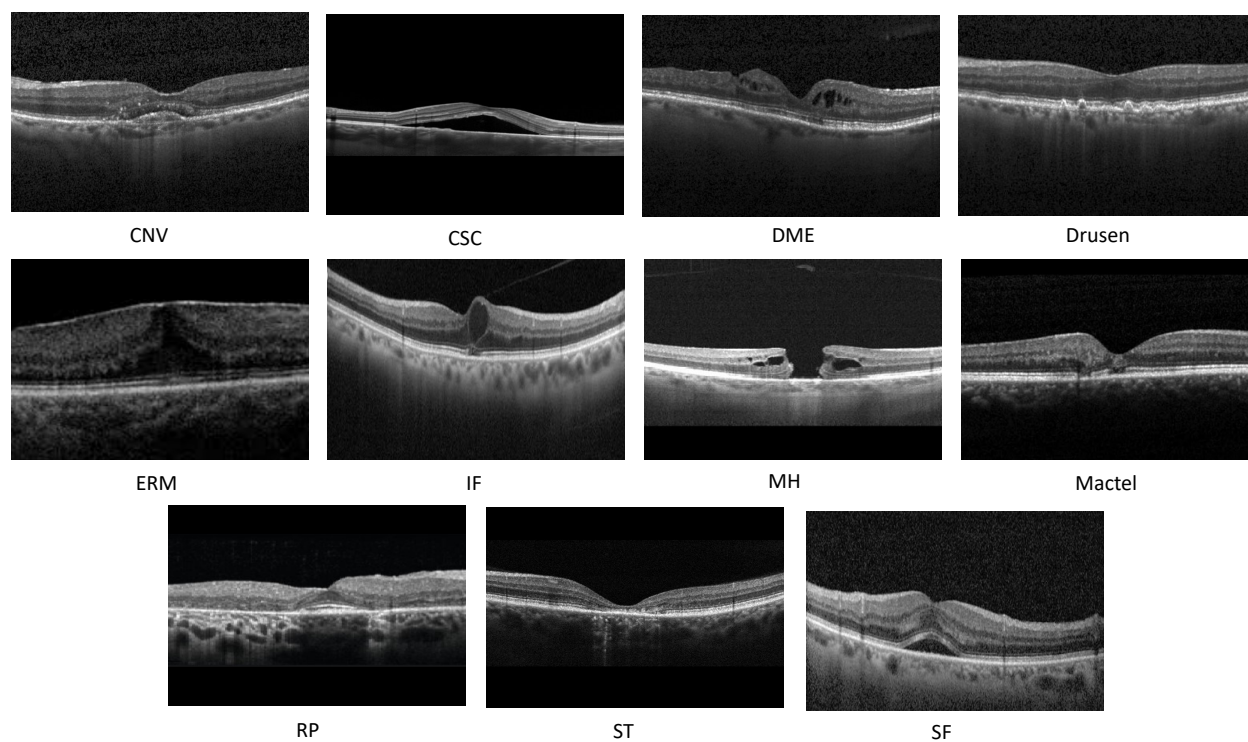


Fig. 2 OCT abnormalities [11]

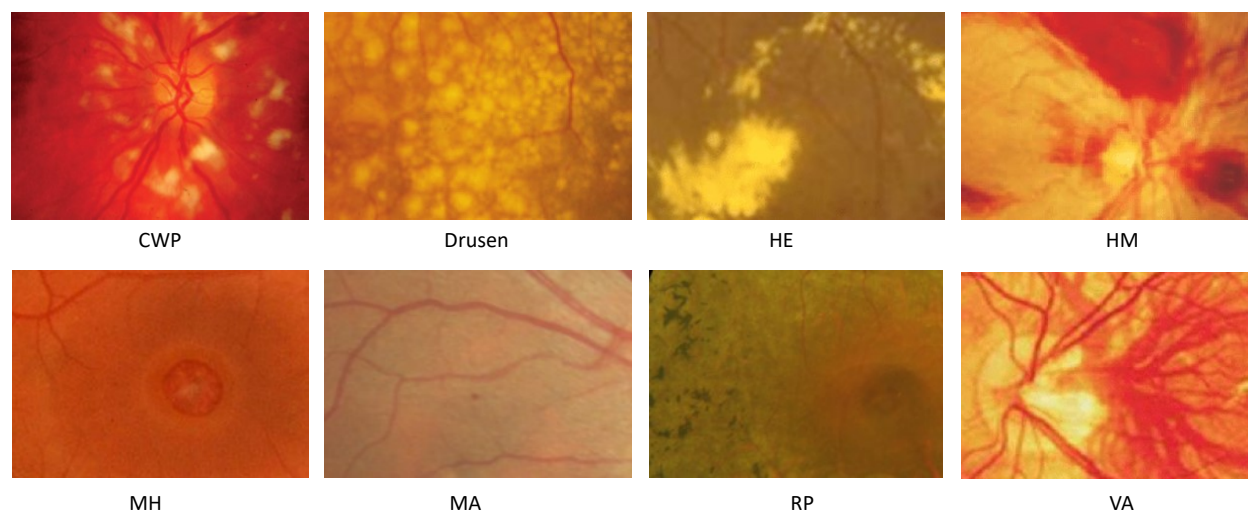


Fig. 3 Fundus abnormalities [28]

the softmax operation. Each submodel outputs a probability vector for all the abnormalities.

The Diagnosis Model consists of two stages: Stage D1 and Stage D2.

In Stage D1, we determine the severity level for each disease from the probability vectors from the Abnormity Models. We use Abnormity-to-Disease Deduction Criteria (shown in Fig. 4) as ground truth. There are multiple submodels in Stage D1 and each one corresponds to one disease. Based on the deduction criteria, we deter-

mine the number of abnormalities for one disease and use the number to define the severity levels. For example, there are totally 5 abnormalities that are present in the disease “rDR”: OCT abnormality “DME” and Fundus abnormalities “HM”, “VA”, “MA”, and “CWP”. Therefore, taking into account the healthy status, we end up with 6 severity levels for disease “rDR”.

We use the fused vector as an input for each submodels in Stage D1, and have the vector go through a FC layer with softmax operation to yield severity level probability vectors.

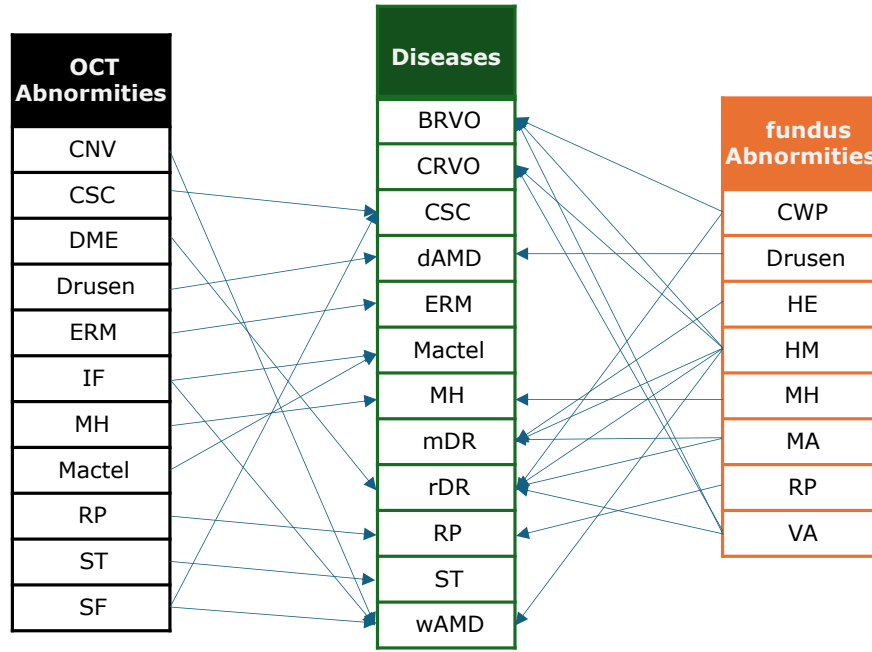


Fig. 4 Abnormity-to-disease Deduction Criteria

In Stage D2, we determine the final disease probability vector. Similarly, we use a fused vector from the outputs of submodels in Stage D1, and have the vector go through a FC layer with softmax operation. The result presents potential diseases that can be referenced by ophthalmologists.

In the MAAM, we leverage the fusion operation to incorporate all the results from different submodels. As shown in Fig. 5, there are totally 3 fusion operations in MAAM.

The first fusion occurs at the output of OCT Model or Fundus Model. In real scenarios, multiple OCT and Fundus images can be used for oc-

ular disease diagnosis. Each image goes through either the OCT Model or the Fundus Model to yield a probability vector. To use the probability results from all the images, a maximization fusion is implemented for all the vectors so that the fusion yields one OCT abnormality probability vector and one Fundus abnormality probability vector with maximum values.

The second fusion occurs at the interface between Abnormity Model and Stage D1. A concatenation fusion is implemented for OCT abnormality

probability vector and Fundus abnormality probability vector. The fused vector works as an input to all the submodels in Stage D1.

The third fusion occurs at the interface between Stage D1 and Stage D2. We concatenate all the severity level vectors to feed the model in Stage D2. The fused vector goes through the FC layer and undergoes a softmax operation to yield the final result.

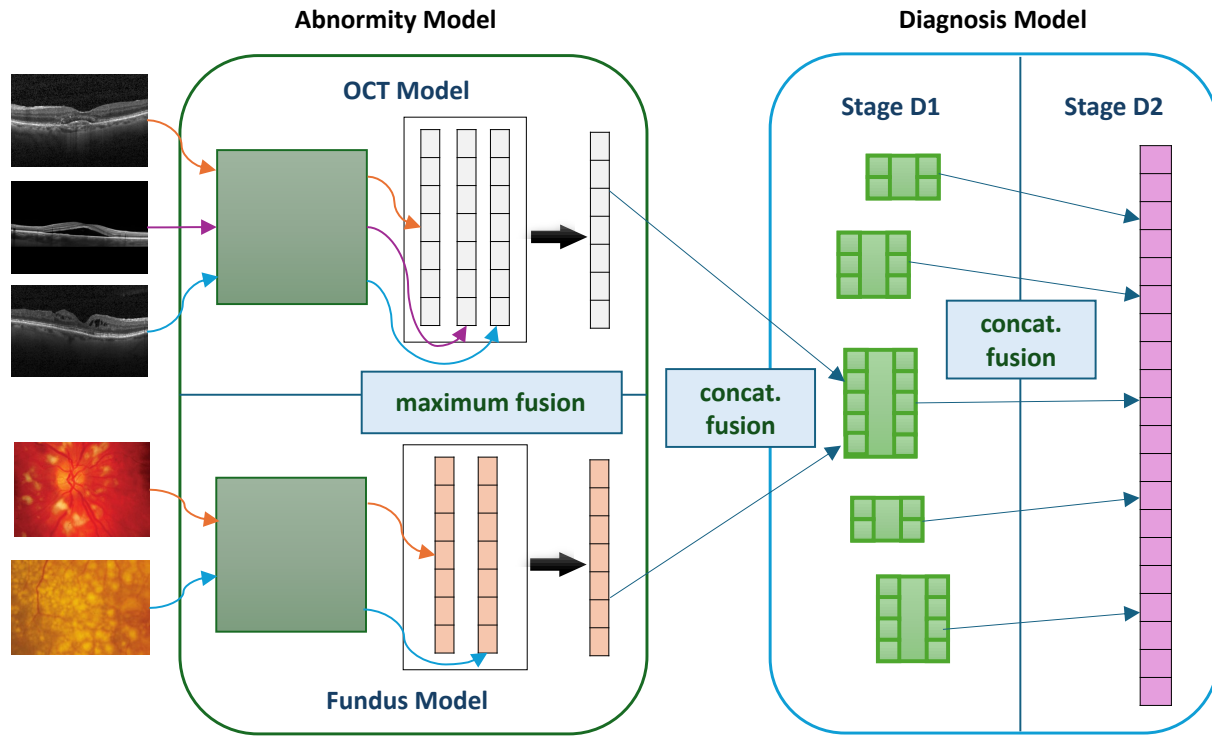


Fig. 5 Fusion mechanism

3 Abnormity Models

3.1 Data Preparation

The images and labels used for training are mainly downloaded from public databases, but some abnormalities are not included in these databases. For those abnormalities, we use the

search engine as an additional data source to get images. The numbers of images acquired from each data source are shown in Table 1 and Table 2. As to the links of the images from the search engine, refer to “Appendix”.

For OCT abnormalities with less than 1000 images, we use Cycle-GAN [32] to generate new im-

ages. We train a Cycle-GAN network to interconvert healthy and abnormality images, take out the generator that converts healthy to abnormality images, and use it to generate new abnormality images. We go through all generated images and adopt those that clearly display only the abnormality of interest. The adoption rates are shown

in Table 3. Fundus images are not generated using Cycle-GAN because generated fundus images are too blurry; in addition, fundus abnormalities are usually less salient than OCT ones and cannot be properly learned by Cycle-GAN, given that we only have a small number of fundus images.

Table 1 OCT Data sources

Abnormality	Source				Total
	1	2	3	4	
CNV	2984	-	-	-	2984
CSC	-	102	32	-	134
DME	2500	-	-	-	2500
Drusen	2500	-	-	-	2500
ERM	-	-	-	16	16
IF	1097	-	-	-	1097
MH	-	99	31	-	130
Mactel	-	-	29	-	29
Healthy	5000	-	-	-	5000
RP	-	102	31	-	133
ST	-	-	23	-	23
SF	1083	-	-	-	1083

1. Normal Disease Database [13]
2. OCTID [10]
3. Few-shot [31]
4. Search engine

Table 2 Fundus Data sources

Abnormality	Source						Total
	1	2	3	4	5	6	
CWP	-	-	-	33	205	-	238
Drusen	-	-	-	50	-	-	50
HE	20	-	-	75	284	-	379
HM	13	66	-	105	278	-	462
MH	-	-	-	-	-	34	34
MA	55	-	-	1	219	-	275
Healthy	100	37	15	-	-	-	152
RP	-	22	-	-	-	44	66
VA	-	64	-	14	-	-	78

1. E-optha [20].
2. Kaggle1000 [1]
3. HRF [22]
4. STARE [2]
5. EyePACS [3]
6. Search engine

Table 3 Adoption rates of Cycle-GAN-generated OCT images

Abnormality	Original	Generated	Adopted	Adoption Rate
CSC	134	3000	1730	58.667%
ERM	19	3000	1931	64.367%
MH	130	3000	1811	60.367%
Mactel	29	3000	1900	63.333%
RP	133	3000	1923	63.100%
ST	23	3000	2572	86.067%

We split the images, including generated images, into training and test datasets, and implement a set of transformations on the images, including horizontal flips, random brightness changes from -10% to +10%, random horizontal and vertical translations between -5% and +5%, random scaling between -20% and +20%, and random rotations, which are between -10° and $+10^\circ$ for OCT images and between -30° and $+30^\circ$ for fundus images. The rotation is only applied to images in the train dataset. Eventually, we get 5000 train images and 500 test images for each OCT abnormality, and 3000 train images and 300 test images for each fundus abnormality.

3.2 Training

The model training is on a desktop computer with Intel® Xeon® Platinum 8352V Processor, 256GB of RAM and 2 NVIDIA GPU (GeForce RTX 4090) with 48GB VRAM. The training uses cross entropy loss, ADAM optimizer with learning rate 0.001, a batch size of 32 and five-fold cross-validation. The code is written with PyTorch in an Anaconda environment. Refer to “Appendix” for the link to the code repository on GitHub.

For the Abnormality Models, we employ a strategy of transfer learning to finetuning.

In the transfer learning phase, pretrained weights from ImageNet [15] are used. We freeze the weights in all the convolutional layers and only vary the weights in the final FC layer. The training lasts for 100 epochs. Every 10 epochs, weights of the model with the best validation accuracy are saved. In order to prevent overfitting on the train dataset, we introduce a measure called overall accuracy, which is the weighted average of validation and test accuracy. For all the saved models, we calculate the overall accuracy to select the

model with the best overall performance on the validation and test datasets, and start finetuning based on this model.

In the finetuning phase, we start from the best model in the transfer learning phase, unfreezing all weights in the model. We train the model for 30 epochs. Similarly, we save the weights of the model with the best validation accuracy every 10 epochs, and find the model with the highest overall accuracy. Finally, we compare the overall accuracies of the best model in the transfer learning phase and the finetuning phase to determine the best model of all.

For both OCT and Fundus Models, we trained 4 commonly used CNNs: ResNet152, ResNet50, ResNet18, and VGG16. The accuracies and losses during training and validation phases are shown in Fig. 6.

We can observe that finetuning significantly increases the model accuracy and, therefore, all the final models are finetuned models. As shown in Table 4, the best CNN for OCT Model is ResNet50 and the best for Fundus Model is ResNet152. ResNet50 performed better than ResNet152 on OCT, possibly because it has fewer parameters and is less likely to overfit on OCT images, which has fewer and clearer traits; on the other hand, ResNet152 is better on fundus possibly because it has more parameters and can better discern the complex traits in fundus images. ResNet18 may have too few parameters, so it performs less well over all; and VGG16 sometimes experiences large dips in accuracy, possibly due to gradient vanishing, and this impairs its performance.

After all the training and comparisons, we determine to use a finetuned model with ResNet50 for OCT Model and a finetuned model with ResNet152 for Fundus Model.

Table 4 Overall accuracies using different CNNs

Model	ResNet152	ResNet50	ResNet18	VGG16
OCT Model	91.906%	92.183%	91.011%	89.744%
Fundus Model	89.111%	88.926%	86.605%	79.185%

Table 5 Test results of the OCT Model

Abnormities	Precision	Sensitivity	Specificity	F1 Score	AUC
CNV	0.990	0.991	0.886	0.990	0.993
CSC	0.995	0.996	0.940	0.995	0.998
DME	0.997	0.997	0.964	0.997	0.999
Drusen	0.997	0.997	0.966	0.997	0.999
ERM	0.962	0.985	0.570	0.974	0.970
IF	0.989	0.983	0.878	0.986	0.991
MH	0.997	0.977	0.972	0.987	0.996
Mactel	0.982	0.988	0.798	0.985	0.994
Healthy	1.000	0.995	1.000	0.997	1.000
RP	0.993	0.998	0.926	0.996	0.999
ST	0.993	0.995	0.924	0.994	0.999
SF	0.996	0.987	0.960	0.992	0.996

Table 6 Test results of the Fundus Model

Abnormities	Precision	Sensitivity	Specificity	F1 Score	AUC
CWP	0.925	0.946	0.390	0.936	0.819
Drusen	0.950	0.992	0.580	0.970	0.959
HE	0.929	0.878	0.460	0.903	0.819
HM	0.921	0.850	0.417	0.884	0.768
MH	0.968	1.000	0.737	0.984	0.999
MA	0.921	0.943	0.353	0.932	0.869
Healthy	0.992	0.970	0.940	0.981	0.988
RP	0.999	0.999	0.990	0.999	1.000
VA	0.946	0.975	0.553	0.960	0.960

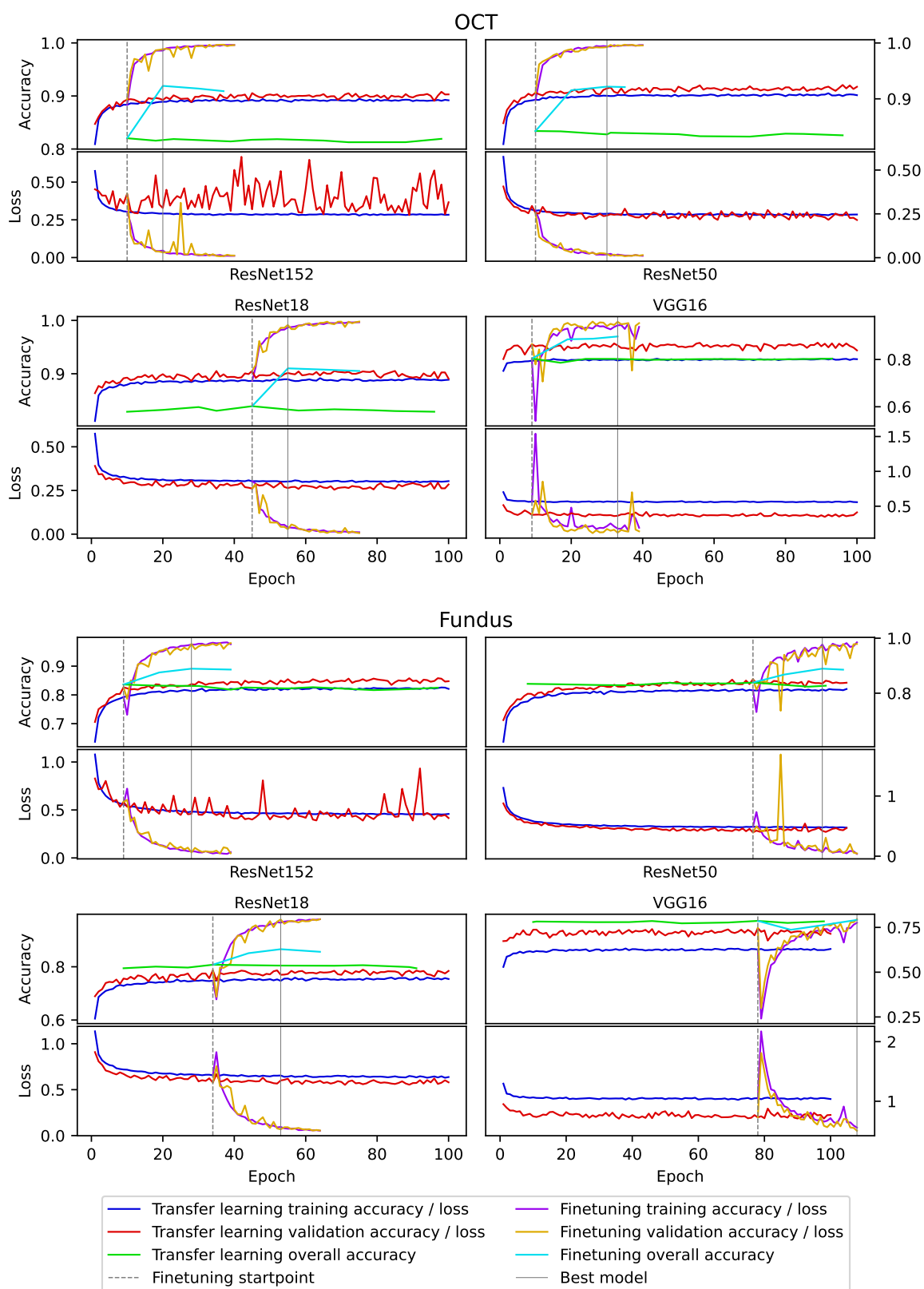


Fig. 6 Abnormity Models training

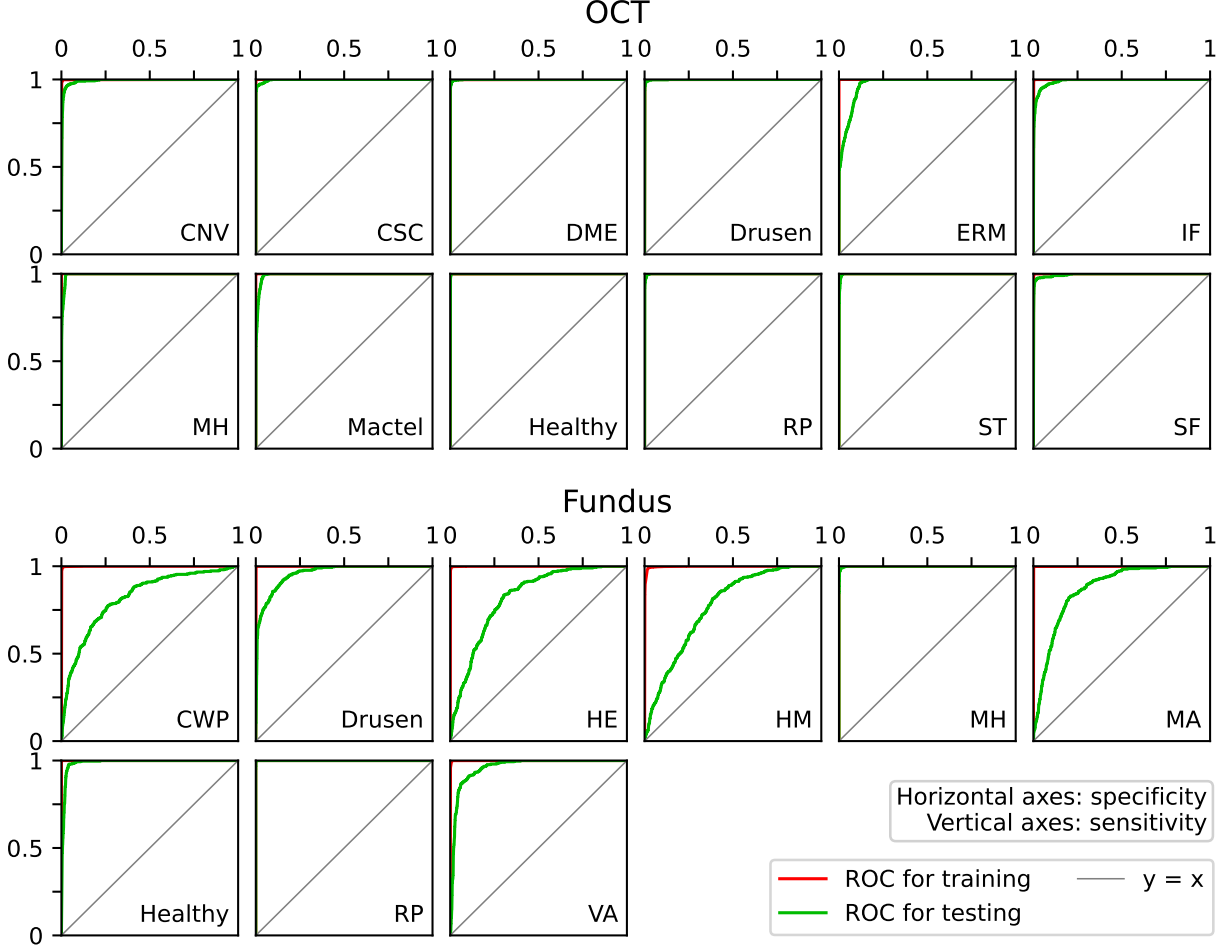


Fig. 7 ROCs of the Abnormity Models

3.3 Results

Table 5 and Table 6 show the predictive values on the test dataset. Fig. 7 shows the ROCs, Fig. 8 shows the confusion matrices and Fig. 9 shows the t-SNE graphs for each abnormality.

The OCT Model tends to overfit, while the Fundus Model cannot reach a satisfying level in terms of DL. Overall, the performance of the OCT Model is significantly better than that of the Fundus Model.

Fundus abnormalities tend to be less prominent than those of OCT, since the abnormality in fundus image are usually quite small and scattered. Moreover, one fundus image usually contains more than one abnormality, while most OCT images contain only one abnormality per image. Also, given that we have fewer fundus images than OCT ones, the difficulties for fundus classification increases.

In order to allow the Abnormity Models to

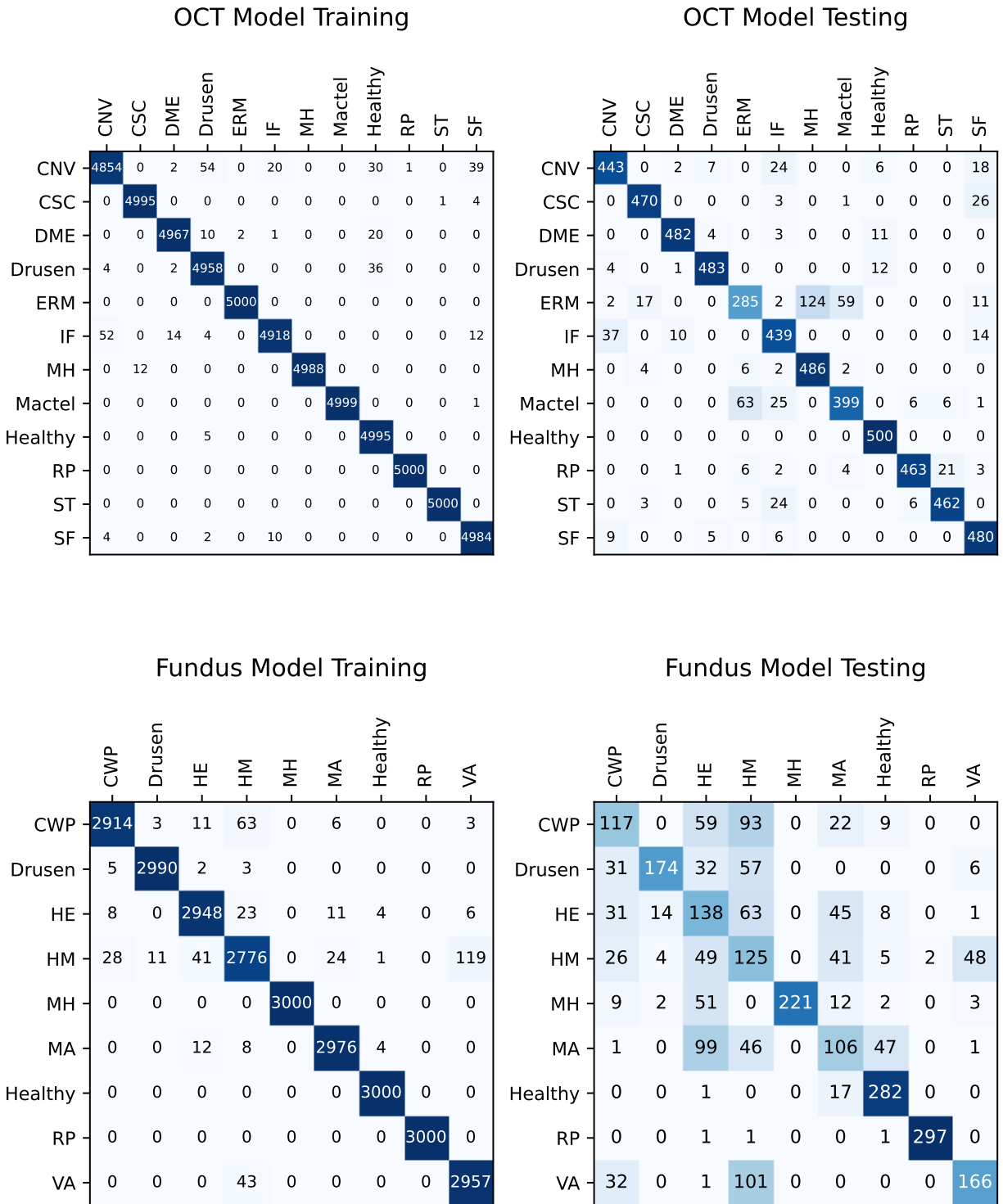


Fig. 8 Confusion matrices of the Abnormity Models

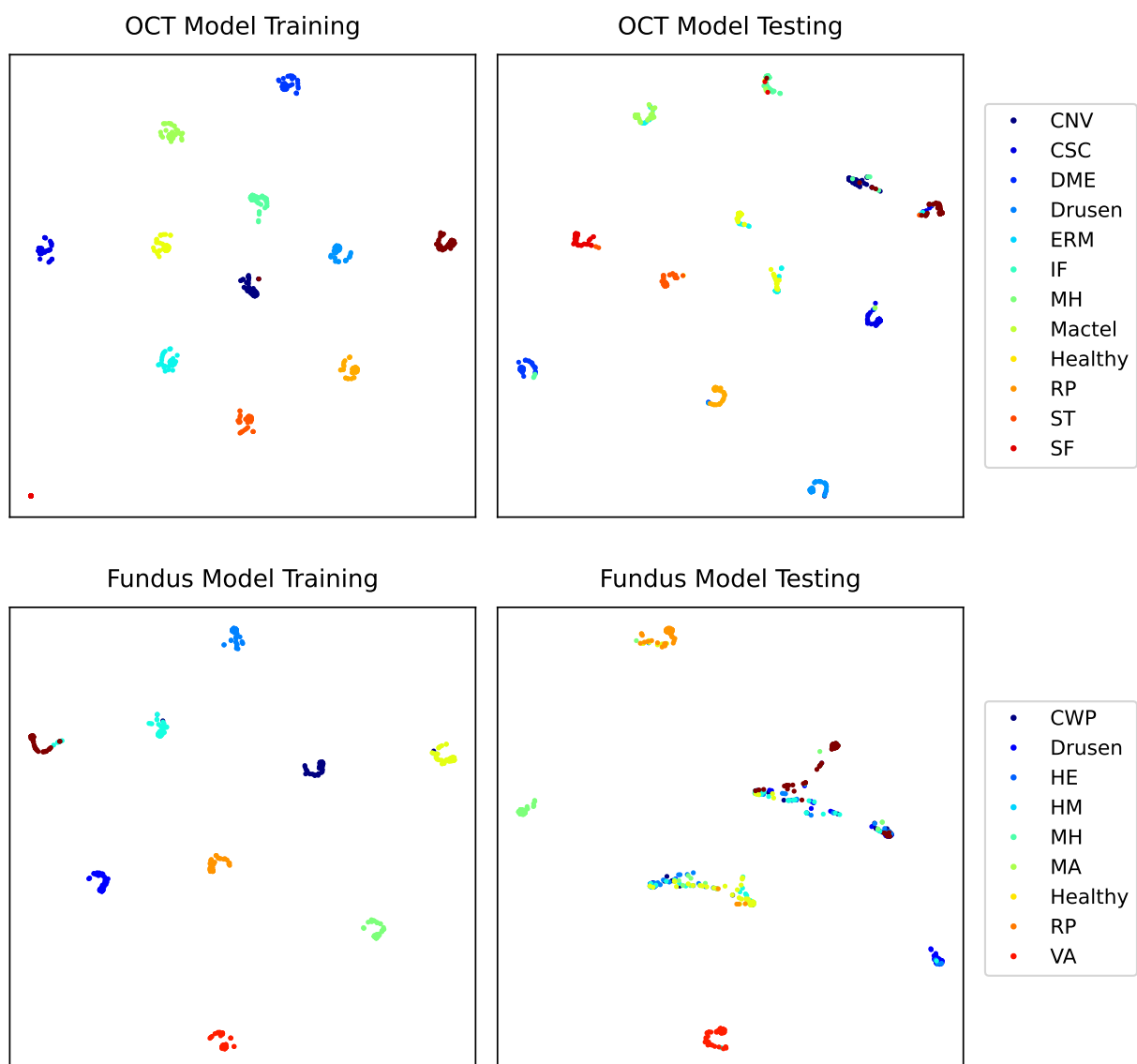


Fig. 9 t-SNE graph of the Abnormity Models

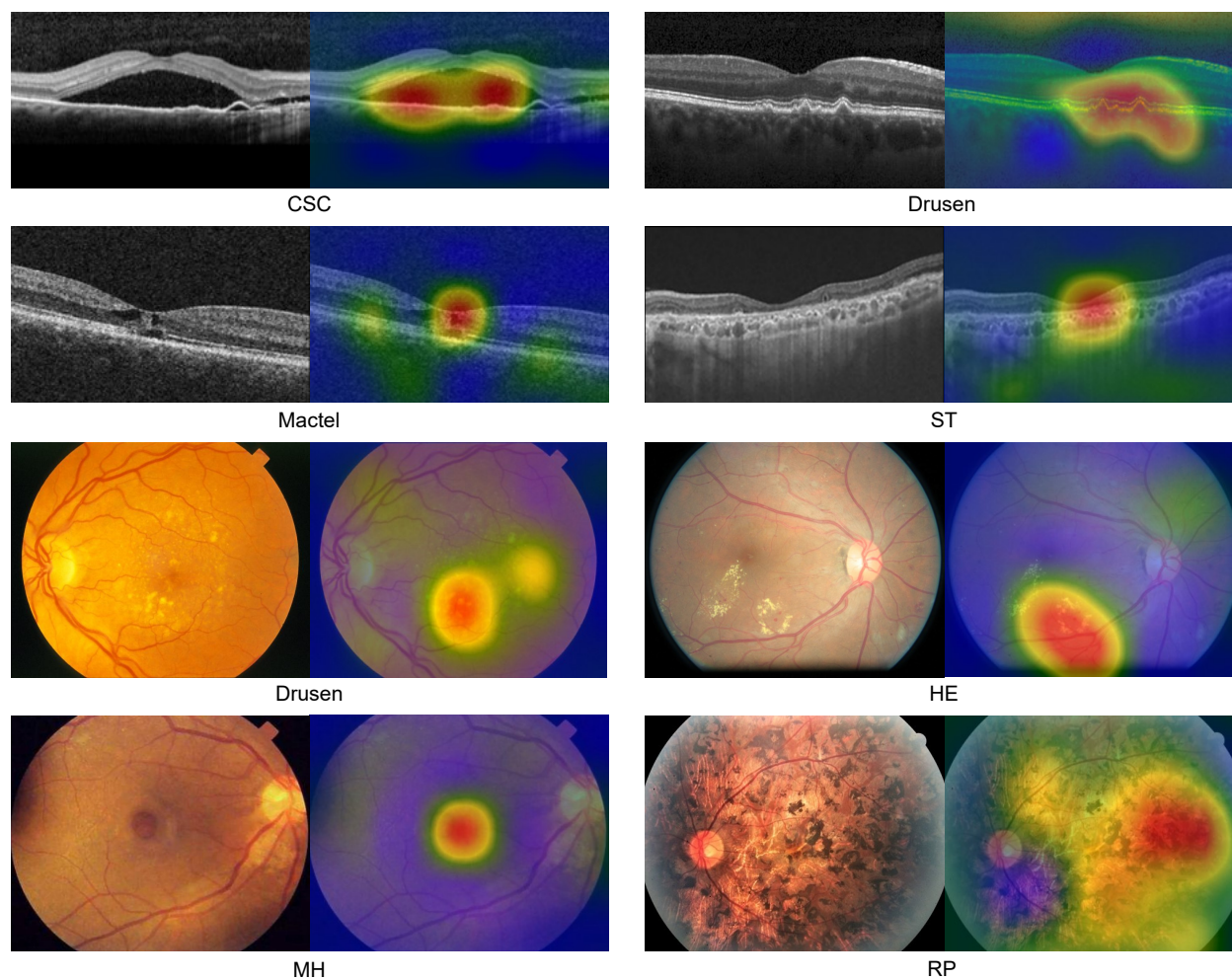


Fig. 10 Grad-CAM highlighting of abnormalities

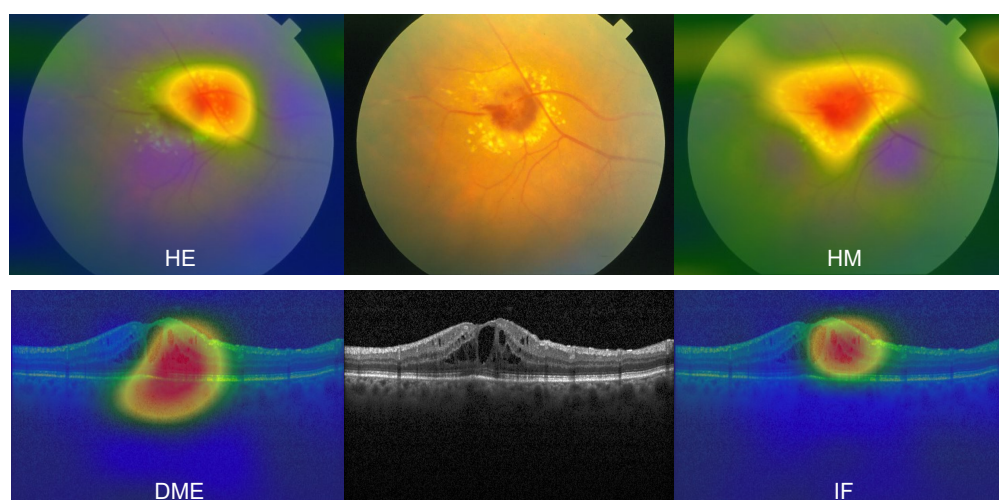


Fig. 11 Grad-CAM highlighting of multiple abnormalities

identify multiple abnormalities in one image, we employ a method to determine the codominant abnormalities. We input an image to the Abnormity Models and get the abnormity probabilities vector. If the abnormity with the highest probability has probability greater than 0.9, it is regarded as dominant; if not, we continue taking the abnormity with the next high probability until either the sum of the probabilities of the chosen abnormalities reaches 0.9, or the number of abnormalities reaches the maximum, which is 4, and all the chosen abnormalities are regarded as codominant.

We can use Grad-CAM [24] to highlight areas on the image that make a large contribution to the final classification. If the model had been trained correctly, this would be equivalent to highlighting the abnormity. In Fig. 10, the left image in each pair of images is the original OCT or Fundus image, and the right one is the image with the abnormity correctly highlighted with Grad-CAM.

Furthermore, Grad-CAM can highlight any designated abnormity, so it can be used to highlight codominant abnormalities. In Fig. 11, the middle images are the original OCT and fundus images. In the images on the left and right, we use Grad-CAM to highlight the codominant abnormalities.

4 Diagnosis Model

4.1 Data Preparation

The purpose of Stage D1 is to determine the severity level for all diseases, each of which has a corresponding submodel. We prepare data for each submodel according to the Abnormity-to-Disease Deduction Criteria (shown in Fig. 4). As stated in Section 2, we determine the target abnormalities for one disease and use the number of

target abnormalities to define the severity levels. If a disease has 5 target abnormalities, then, taking into account the healthy status, we get 6 severity levels, namely 0 to 5. We use sets of images as inputs to the submodel, and the severity level label for one set is equal to the number of target abnormalities that appear in the set. We randomly choose sets of images from the OCT and fundus images and determine the severity level for each set. In the end, we get 10000 inputs for training and 10000 inputs for testing for each severity level.

The purpose of Stage D2 is to output the disease probability vectors. For each disease, we use the Abnormity-to-Disease Deduction Criteria to find the target abnormalities, randomly choose sets of images where each of them is from one target abnormity, and label the sets of images with the disease. We get 10000 sets of images for training and 10000 sets of images for testing for each of the disease.

4.2 Training

The Diagnosis Model is trained with the same hardware as the Abnormity Models. Stage D1 submodels are trained for 10 epochs and Stage D2 model is trained for 30 epochs, and all the other hyperparameters are identical to those of the Abnormity Models. Refer to Section 3.2 for details.

Submodels in Stage D1 and the model in Stage D2 quickly reach very high accuracies during training and validation because there are plenty of training data and the models leverage relatively simpler networks.

4.3 Results

Fig. 12 shows the confusion matrices for Stage D1 and Fig. 13 shows the accuracies of the

submodels of Stage D1. Table 7 shows the predictive values of Stage D2, Fig. 14 shows the ROCs, Fig. 15 shows the confusion matrix and Fig 16 shows the t-SNE graph.

The submodels of Stage D1 tend to yield results where the predicted severity level is 1 level offset from the label. This impairs the accuracies of the submodels of Stage D1. However, Stage D2 partly solves this problem, as the model in Stage D2 has a higher accuracy than the average

accuracy of the Stage D1 submodels.

Stage D2 performs quite well on classifying the diseases. Furthermore, considering that some diseases may look alike each other, we employ a method similar to the codominant abnormalities method to allow Stage D2 to give up to 3 codominant diseases. As shown in Fig. 13, if the codominant diseases method is used, the accuracy of Stage D2 further increases.

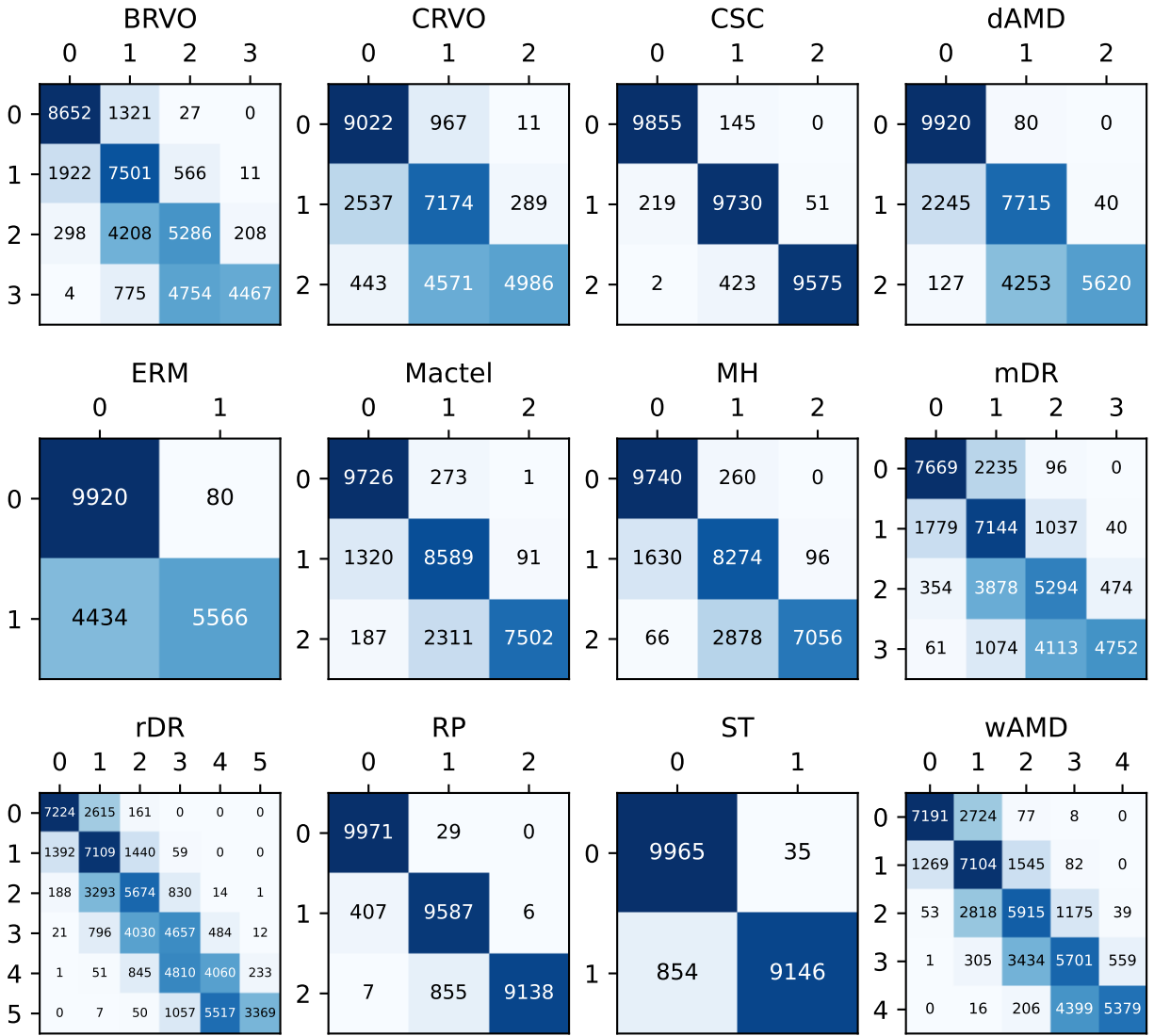


Fig. 12 Confusion matrices of Stage D1

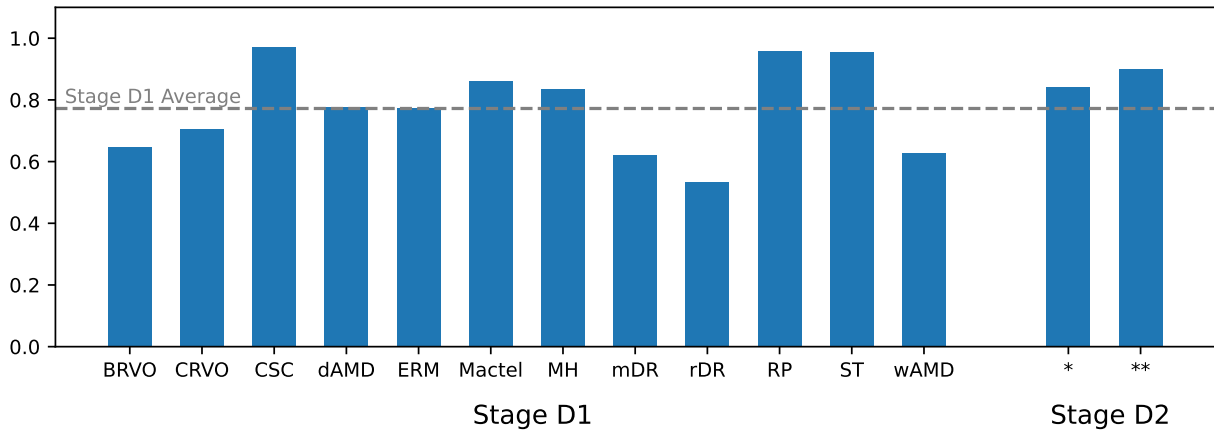


Fig. 13 Accuracies of the Diagnosis Model (*: accuracy in terms of the disease with highest probability; **: accuracy in terms of codominant diseases)

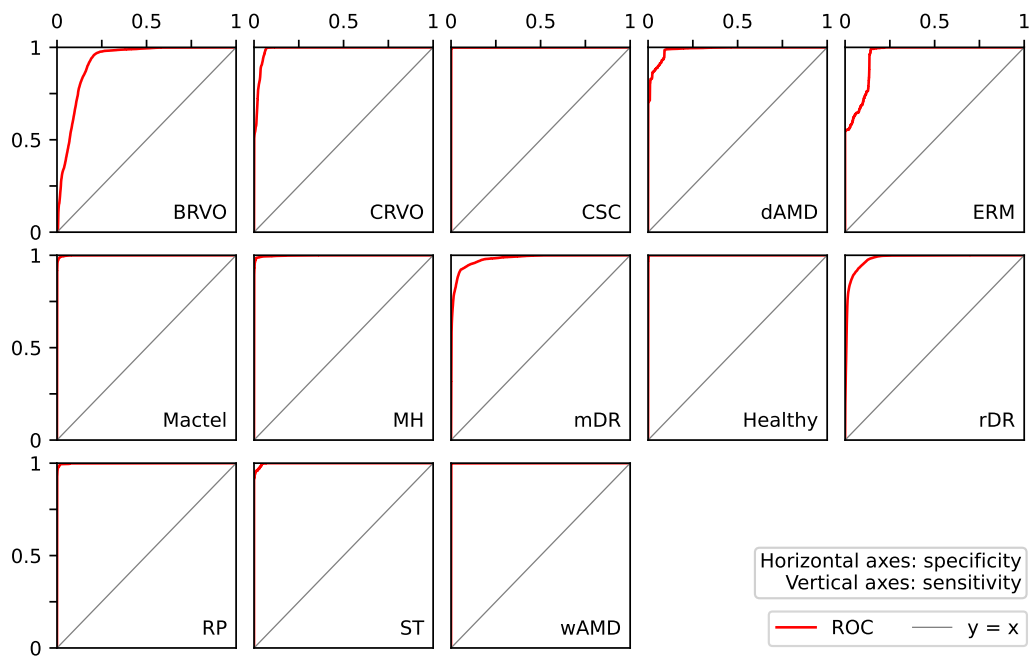


Fig. 14 ROCs of Stage D2

	BRVO	CRVO	CSC	dAMD	ERM	Mactel	MH	mDR	Healthy	rDR	RP	ST	wAMD
BRVO	3947	3428	0	4	0	0	0	1940	10	671	0	0	0
CRVO	1205	7466	0	4	0	0	0	1202	7	116	0	0	0
CSC	0	0	9891	87	0	4	0	0	0	0	0	0	18
dAMD	0	1591	0	8285	0	0	0	16	63	0	0	0	45
ERM	0	113	478	0	5813	1116	2457	0	0	0	0	0	23
Mactel	0	2	45	0	169	9615	0	0	78	0	0	9	82
MH	0	294	3	0	9	50	9547	12	82	0	0	0	3
mDR	421	903	0	89	0	0	0	7938	290	343	0	3	13
Healthy	0	0	0	0	0	0	0	237	9763	0	0	0	0
rDR	203	22	0	1	0	0	0	1760	66	7936	0	0	12
RP	0	41	36	0	0	47	0	0	53	0	9630	193	0
ST	0	0	22	0	112	440	0	0	0	0	0	9426	0
wAMD	0	3	24	2	0	16	0	3	13	0	0	0	9939

Fig. 15 Confusion matrix of Stage D2

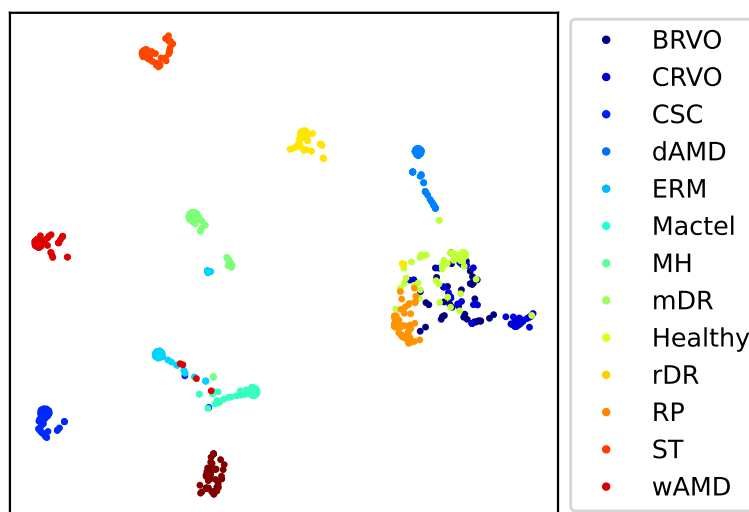


Fig. 16 t-SNE graph of Stage D2

Table 7 Test results of Stage D2

Abnormities	Precision	Sensitivity	Specificity	F1 Score	AUC
BRVO	0.951	0.985	0.395	0.968	0.918
CRVO	0.978	0.947	0.747	0.962	0.986
CSC	0.999	0.995	0.989	0.997	1.000
dAMD	0.986	0.998	0.829	0.992	0.986
ERM	0.966	0.998	0.581	0.982	0.952
Mactel	0.997	0.986	0.962	0.991	0.999
MH	0.996	0.980	0.955	0.988	0.998
mDR	0.982	0.957	0.794	0.969	0.980
Healthy	0.998	0.994	0.976	0.996	1.000
rDR	0.983	0.991	0.794	0.987	0.982
RP	0.997	1.000	0.963	0.998	0.999
ST	0.995	0.998	0.943	0.997	0.998
wAMD	0.999	0.998	0.994	0.999	1.000

5 Discussion

There are some studies working on classifying OCT abnormalities. For examples, Leandro, Lorenzo, Aleksandar, *et al.*'s model is trained on 10770 images (most images belong to multiple classes), classifies 8 abnormalities, and has overall accuracy between 93% and 99% [16]. Li, Chen, Liu, *et al.*'s model is trained on 21357 images, classifies 4 abnormalities, and has overall accuracy 97.3% [18]. And there are some studies working on classifying fundus abnormalities. For example, Son, Shin, Kong, *et al.*'s model is trained on 103262 images, classifies 15 abnormalities, and has a mean AUC of 0.980 [26]. In comparison, our OCT Model is trained on 15632 images, classifies 11 abnormalities, and has overall accuracy less than 80%. And our Fundus Model is trained on 1734 images, classifies 8 abnormalities, and has a mean AUC of 0.909. As a matter of fact, our Abnormity

Models are not satisfying in terms of performance.

Our data are collected from various online sources and therefore lack a uniform standard. Furthermore, some of the data are labeled by ourselves, while we do not have the expertise of ophthalmologists. Moreover, our data is not sufficient. There is also an imbalance between the number of images of different abnormalities. In the OCT Model, the imbalance is partly neutralized by using Cycle-GAN. However, in the Fundus Model, we could only perform transformations to generate more images, which may increase the model's tendency of being overfitting and make it hard for the model to extract the correct features. Also as mentioned before, in our model, there are often multiple abnormalities on one image, which increase the difficulty to identify one specific abnormality correctly.

In MAAM, the Diagnosis Model improves the overall performance successfully. There are also

some studies using similar framework. For example, Son, Shin, Kong, *et al.*'s diagnosis model classifies 8 diseases and has mean AUC 0.992[26]. In comparison, our Diagnosis Model classifies 12 diseases and has mean AUC of 0.984 which is close to other studies.

It is noted that the goal of MAAM is not to identify one specific disease. It is developed for identifying all the potential diseases, which is different from other studies mentioned in this paper. Therefore, we introduced codominant abnormalities and codominant diseases, which buff up the performances. Moreover, the Diagnosis Model performs two additional feature extractions. While the Abnormity Models only have accuracies between 70% and 80%, after we extracted the features of severity levels of diseases in Stage D1, the average accuracy increases. And after we extracted the features of disease in Stage D2, the accuracy keep on increasing up to a satisfying level. These two stages enhance the performance of the Abnormity Models and make the features of the diseases more distinct. Also, in training the Diagnosis Model, we use the Abnormity-to-Disease Deduction Criteria to generate ground truth, which is reliable even without involving ophthalmologists.

6 Conclusion

The main goal of this study is to devise a novel model and verify its feasibility. The MAAM takes both OCT and fundus images as input. We integrate information from different sources by employing the fusion mechanism. Moreover, we deduce disease from abnormalities and simulate the decision-making process of ophthalmologists. We also introduced codominant abnormalities and diseases, providing more information for reference. As a result, the model breaks the black box of

complex neural network and exposes more information. On the other hand, there is some room for improvement, such as gathering more authentic data, introducing the expertise of ophthalmologists, refining the Abnormity-to-Disease Deduction Criteria, and improving the structure of the Diagnosis Model, etc.

References

- [1] en. [Online]. Available: <https://kaggle.com/code/saranga7/1000fundus-pytorch-transferlearning>.
- [2] [Online]. Available: <https://cecas.clemson.edu/~ahoover/stare/>.
- [3] en. [Online]. Available: <https://kaggle.com/competitions/diabetic-retinopathy-detection>.
- [4] V. Andrearczyk and H. Müller, "Deep multimodal classification of image types in biomedical journal figures," en, in *Experimental IR Meets Multilinguality, Multimodality, and Interaction* (Lecture Notes in Computer Science), P. Bellot, C. Trabelsi, J. Mothe, *et al.*, Eds., Lecture Notes in Computer Science. Cham: Springer International Publishing, 2018, vol. 11018, pp. 3–14, ISBN: 978-3-319-98931-0. DOI: 10.1007/978-3-319-98932-7_1. [Online]. Available: http://link.springer.com/10.1007/978-3-319-98932-7_1.
- [5] *Artificial Intelligence and Ophthalmology: Perks, Perils and Pitfalls* (Current Practices in Ophthalmology), en. Singapore: Springer Singapore, 2021, ISBN: 9789811606335. DOI: 10.1007/978-981-16-0634-2. [Online]. Available: <https://link.springer.com/10.1007/978-981-16-0634-2>.

- [6] A. Camino, Z. Wang, J. Wang, *et al.*, “Deep learning for the segmentation of preserved photoreceptors on en face optical coherence tomography in two inherited retinal diseases,” *Biomedical optics express*, vol. 9, no. 7, pp. 3092–3105, 2018.
- [7] T.-C. Chen, W. S. Lim, V. Y. Wang, *et al.*, “Artificial intelligence–assisted early detection of retinitis pigmentosa—the most common inherited retinal degeneration,” *Journal of Digital Imaging*, vol. 34, pp. 948–958, 2021.
- [8] M. Daich Varela, S. Sen, T. A. C. De Guimaraes, *et al.*, “Artificial intelligence in retinal disease: Clinical application, challenges, and future directions,” *Graefe’s Archive for Clinical and Experimental Ophthalmology*, pp. 1–15, 2023.
- [9] L. Fang, C. Wang, S. Li, H. Rabbani, X. Chen, and Z. Liu, “Attention to lesion: Lesion-aware convolutional neural network for retinal optical coherence tomography image classification,” *en, IEEE Transactions on Medical Imaging*, vol. 38, no. 8, pp. 1959–1970, Aug. 2019, ISSN: 0278-0062, 1558-254X. DOI: 10.1109/TMI.2019.2898414.
- [10] P. Gholami, P. Roy, M. K. Parthasarathy, and V. Lakshminarayanan, “Octid: Optical coherence tomography image database,” *en, Computers & Electrical Engineering*, vol. 81, p. 106532, Jan. 2020, ISSN: 00457906. DOI: 10.1016/j.compeleceng.2019.106532.
- [11] *Handbook of retinal OCT*, *en*, Second edition. Philadelphia, PA: Elsevier, 2022, ISBN: 978-0-323-75772-0.
- [12] K. He, X. Zhang, S. Ren, and J. Sun, “Deep residual learning for image recognition,” *en*, in *2016 IEEE Conference on Computer Vision and Pattern Recognition (CVPR)*, Las Vegas, NV, USA: IEEE, Jun. 2016, pp. 770–778, ISBN: 978-1-4673-8851-1. DOI: 10.1109/CVPR.2016.90. [Online]. Available: <http://ieeexplore.ieee.org/document/7780459/>.
- [13] D. Kermany, K. Zhang, and M. Goldbaum, “Large dataset of labeled optical coherence tomography (oct) and chest x-ray images,” *en*, vol. 3, Jun. 2018. DOI: 10.17632/rscbjbr9sj.3. [Online]. Available: <https://data.mendeley.com/datasets/rscbjbr9sj/3>.
- [14] D. S. Kermany, M. Goldbaum, W. Cai, *et al.*, “Identifying medical diagnoses and treatable diseases by image-based deep learning,” *en, Cell*, vol. 172, no. 5, 1122–1131.e9, Feb. 2018, ISSN: 00928674. DOI: 10.1016/j.cell.2018.02.010.
- [15] A. Krizhevsky, I. Sutskever, and G. E. Hinton, “Imagenet classification with deep convolutional neural networks,” *en, Communications of the ACM*, vol. 60, no. 6, pp. 84–90, May 2017, ISSN: 0001-0782, 1557-7317. DOI: 10.1145/3065386.
- [16] I. Leandro, B. Lorenzo, M. Aleksandar, G. Rosa, A. Agostino, and T. Daniele, “Oct-based deep-learning models for the identification of retinal key signs,” *Scientific Reports*, vol. 13, no. 1, p. 14628, 2023.
- [17] B. Li, H. Chen, B. Zhang, *et al.*, “Development and evaluation of a deep learning model for the detection of multiple fundus diseases based on colour fundus photography,” *British Journal of Ophthalmology*, vol. 106, no. 8, pp. 1079–1086, 2022.

- [18] F. Li, H. Chen, Z. Liu, *et al.*, “Deep learning-based automated detection of retinal diseases using optical coherence tomography images,” *Biomedical optics express*, vol. 10, no. 12, pp. 6204–6226, 2019.
- [19] T. Y. A. Liu, C. Ling, L. Hahn, C. K. Jones, C. J. Boon, and M. S. Singh, “Prediction of visual impairment in retinitis pigmentosa using deep learning and multimodal fundus images,” *British Journal of Ophthalmology*, vol. 107, no. 10, pp. 1484–1489, 2023.
- [20] G. MAFFRE, G. PATRY, B. GAUTHIER, *et al.*, *E-ophta*, en. [Online]. Available: <https://www.adcis.net/en/third-party/e-ophta/>.
- [21] H. Masumoto, H. Tabuchi, S. Nakakura, *et al.*, “Accuracy of a deep convolutional neural network in detection of retinitis pigmentosa on ultrawide-field images,” *PeerJ*, vol. 7, e6900, 2019.
- [22] J. Odstroicilik, R. Kolar, A. Budai, *et al.*, “Retinal vessel segmentation by improved matched filtering: Evaluation on a new high-resolution fundus image database,” en, *IET Image Processing*, vol. 7, no. 4, pp. 373–383, Jun. 2013, ISSN: 1751-9667, 1751-9667. DOI: 10.1049/iet-ipr.2012.0455.
- [23] O. Ronneberger, P. Fischer, and T. Brox, “U-net: Convolutional networks for biomedical image segmentation,” en, no. arXiv:1505.04597, May 2015, arXiv:1505.04597 [cs]. [Online]. Available: <http://arxiv.org/abs/1505.04597>.
- [24] R. R. Selvaraju, M. Cogswell, A. Das, R. Vedantam, D. Parikh, and D. Batra, “Grad-cam: Visual explanations from deep networks via gradient-based localization,” en,
- [25] K. Simonyan and A. Zisserman, “Very deep convolutional networks for large-scale image recognition,” en, no. arXiv:1409.1556, Apr. 2015, arXiv:1409.1556 [cs]. [Online]. Available: <http://arxiv.org/abs/1409.1556>.
- [26] J. Son, J. Y. Shin, S. T. Kong, *et al.*, “An interpretable and interactive deep learning algorithm for a clinically applicable retinal fundus diagnosis system by modelling finding-disease relationship,” en, *Scientific Reports*, vol. 13, no. 1, p. 5934, Apr. 2023, ISSN: 2045-2322. DOI: 10.1038/s41598-023-32518-3.
- [27] P. P. Srinivasan, L. A. Kim, P. S. Mettu, *et al.*, “Fully automated detection of diabetic macular edema and dry age-related macular degeneration from optical coherence tomography images,” *Biomedical optics express*, vol. 5, no. 10, pp. 3568–3577, 2014.
- [28] S. Wolf, B. Kirchhof, and M. Reim, *The ocular fundus: from findings to diagnosis*, en. Stuttgart: Thieme, 2006, ISBN: 978-3-13-139371-5.
- [29] Z. Xu, W. Wang, J. Yang, *et al.*, “Automated diagnoses of age-related macular degeneration and polypoidal choroidal vasculopathy using bi-modal deep convolutional neural networks,” en, *British Journal of Ophthalmology*, vol. 105, no. 4, pp. 561–566, Apr. 2021, ISSN: 0007-1161, 1468-2079. DOI: 10.1136/bjophthalmol-2020-315817.
- [30] T. K. Yoo, J. Y. Choi, and H. K. Kim, “Feasibility study to improve deep learning in oct diagnosis of rare retinal diseases with few-shot classification,” *Medical & Biological Engineering & Computing*, vol. 59, pp. 401–415, 2021.

- [31] T. Yoo, "Data for: Improved accuracy in oct diagnosis of rare retinal disease using few-shot learning with generative adversarial networks," en, vol. 2, Oct. 2020. DOI: 10.17632/btv6yrdbmv.2. [Online]. Available: <https://data.mendeley.com/datasets/btv6yrdbmv/2>.
- [32] J.-Y. Zhu, T. Park, P. Isola, and A. A. Efros, "Unpaired image-to-image translation using cycle-consistent adversarial networks," en, no. arXiv:1703.10593, Aug. 2020, arXiv:1703.10593 [cs]. [Online]. Available: <http://arxiv.org/abs/1703.10593>.

Appendix

Code

The link for the GitHub repository is <https://github.com/SiqiPan2008/MAAM/>.

Abnormities and Diseases

OCT Abnormities

Abnormity	Abbr.	Description
Choroidal neovascularization	CNV	The abnormal growth of new blood vessels in the choroid layer.
Central serous chorioretinopathy	CSC	The accumulation of fluid underneath the retina.
Diabetic macular edema	DME	The accumulation of fluid in the macula associated with diabetic retinopathy.
Drusen	Drusen	Small deposits of extracellular material that accumulate beneath the retinal pigment epithelium (RPE) or between the RPE and the photoreceptor layer in the macular region of the retina.
Epiretinal membrane	ERM	A thin layer of fibrous tissue forms on the surface of the retina, particularly the macula.
Intraretinal fluid	IF	The accumulation of fluid within the layers of the retina.
Macular hole	MH	Disruption or discontinuity in the normal retinal layers surrounding the macular hole.
Macular telangiectasia	Mactel	Abnormalities in the macular blood vessels, leading to changes in the macular structure and function.
Retinitis pigmentosa	RP	Thinning of the retinal layers. Disruption of photoreceptor layers. Attenuation of retinal vasculature.
Stargardt disease	ST	Thinning and atrophy of the retina. Disruption of photoreceptor layers. Presence of subretinal deposits.
Subretinal fluid	SF	The accumulation of fluid between the neurosensory retina and the retinal pigment epithelium (RPE)

Fundus Abnormalities

Abnormity	Abbr.	Description
Cotton wool patch	CWP	White or off-white lesions. Irregular shapes and margins. Also called soft exudates.
Drusen	Drusen	Small, round or oval-shaped yellow or white deposits.
Hard exudate	HE	Yellow or Yellow-White Deposits. Hard Borders. Distribution. Clustering Around Blood Vessels

Hemorrhage	HM	Small dot-like to larger blot. Fresh hemorrhages typically appear bright red or deep red in color, indicating the presence of oxygenated blood. Over time, as the blood undergoes degradation and clotting, the hemorrhage may change color to darker red, orange, or yellowish hues.
Macular hole	MH	Full-thickness macular hole showing a surrounding cuff of subretinal fluid.
Microaneurysm	MA	Small vascular dilatations observed in retinal blood vessels, visible as tiny red dots scattered in the retina posteriorly.
Retinitis pigmentosa	RP	Arteriolar attenuation. Retinal pigmentary changes (either hypopigmentation and/or hyperpigmentation in the form of bone-spicule and pigment clumpings). Waxy disc pallor.
Vascular abnormality	VA	Retinal Vessel Tortuosity. Retinal Vessel Caliber Changes.

Diseases

Disease	Abbr.
Branch or hemi-central retinal vein occlusion	BRVO
Central retinal vein occlusion	CRVO
Central serous chorioretinopathy	CSC
Dry age-related macular degeneration	dAMD
Epiretinal membrane	ERM
Macular telangiectasia	Mactel
Macular hole	MH
Mild diabetic retinopathy	mDR
Referable diabetic retinopathy	rDR
Retinitis pigmentosa	RP
Stargardt disease	ST
Wet age-related macular degeneration	wAMD

Image Sources

OCT – ERM

1. <https://qers.com.au/eye-conditions/epiretinal-membrane-erm/>
2. <https://www.asrs.org/patients/retinal-diseases/19/epiretinal-membranes>
3. <https://theretinagroup.com/epiretinal-membrane/>
4. <https://www.istanbulretina.com/en-diseases-epiretinal-membrane.php>
5. <https://www.mdfoundation.com.au/about-macular-disease/other-macular-conditions/epiretinal-membrane-macular-pucker/>

6. https://www.researchgate.net/figure/Grading-of-epiretinal-membrane-ERM-by-spectral-domain-optical-coherence-tomography_fig1_351426760
7. <https://www.singhealth.com.sg/patient-care/conditions-treatments/epiretinal-membrane>
8. <https://www.windycityretina.com/epiretinal-membrane/>
9. <https://retinacentertx.com/conditions/macular-pucker>
10. <https://www.rvscny.com/patient-eduction/conditions-we-treat/epiretinal-membrane/>
11. <https://www.lyneye.co.za/epiretinal-membrane-erm/>
12. <https://rehmansiddiqui.com/epi-retinal-membrane-erm/>
13. <https://www.reviewofophthalmology.com/article/when-and-how-to-peel-an-epiretinal-membrane>
14. <https://www.janigianretina.com/retina-conditions/epiretinal-membrane>
15. https://www.researchgate.net/figure/6-months-later-ERM-with-partial-attachment-to-the-retina_fig2_309566437
16. <https://www.capefearretina.com/epiretinal-membrane/>

Fundus – MH

1. <https://emedicine.medscape.com/article/1224320-overview>
2. <https://www.chatswoodeye.com/macular-hole-specialists/>
3. <https://swretina.com/macular-hole/>
4. <https://www.opthalmologyexpertservices.com/blog/2019/macular-hole>
5. https://www.researchgate.net/publication/38109568_Bilateral_macular_hole_secondary_to_remote_lightning_strike
6. https://www.researchgate.net/publication/38109568_Bilateral_macular_hole_secondary_to_remote_lightning_strike
7. <https://www.reviewofoptometry.com/article/facedown-showdown>
8. <https://www.gotzaridis.gr/en/conditions/macula/full-thickness-macular-hole>
9. https://www.researchgate.net/figure/Fundus-image-of-the-right-eye-of-case-1-a-shows-a-macular-hole-with-associated-retinal_fig1_324657341

10. <https://www.girayersoz.com.tr/en/macular-hole/>
11. <https://www.gotzaridis.gr/en/conditions/macula/full-thickness-macular-hole>
12. <https://www.gotzaridis.gr/en/conhttps://www.willseye.org/macular-hole/ditions/macula/full-thickness-macular-hole>
13. <https://www.willseye.org/macular-hole/>
14. <http://www.oculist.net/downaton502/prof/ebook/duanes/pages/v3/ch031/013f.html>
15. <https://www.slideshare.net/slideshow/macular-hole-227845841/227845841#11>
16. <https://www.slideshare.net/slideshow/macular-hole-227845841/227845841#12>
17. <https://www.jaypeedigital.com/book/9788180616532/chapter/ch7>
18. <https://emedicine.medscape.com/article/1224320-clinical?form=fpf>
19. <https://www.jaafarelannanmd.com/macular-hole>
20. <https://asiaeyecentre.com.sg/eye-conditions/the-ageing-eye/macular-hole/>
21. <https://retinaandeye.com.au/eye-conditions/full-thickness-macular-holes/>
22. <https://retinahi.com/interesting-cases/>
23. <https://imagebank.asrs.org/file/2858/traumatic-macular-hole>
24. <https://www.semanticscholar.org/paper/Giant-macular-hole-as-an-atypical-consequence-of-a-Blaise-Comhaire/5c9a60375d904323eb5fbcd52b6bd03b735f6951>
25. <https://webeye.ophth.uiowa.edu/eyeforum/atlas/pages/Macular-hole-commotio-retinae-choroidal-rupture.htm#gsc.tab=0>
26. <https://areaoftalmologica.com/en/terms-of-ophthalmology/macular-hole/>
27. <https://www.reviewofoptometry.com/article/facedown-showdown>
28. <https://montanaretinaconsultants.com/portfolio/macular-holes/>
29. <https://ccteyes.com/2019/09/30/what-is-a-macular-hole-and-how-does-it-affect-our-vision/>
30. <https://www.backoftheeyemd.com/retina-services/macular-holes/>
31. [https://www.asrs.org/content/images/cms/image_rib_macularhole_2_2858.jpg/image-full;size\\$250,194.ImageHandler](https://www.asrs.org/content/images/cms/image_rib_macularhole_2_2858.jpg/image-full;size$250,194.ImageHandler)
32. [https://www.asrs.org/content/images/cms/image_rib_macularhole_2_2858.jpg/image-full;size\\$250,194.ImageHandler](https://www.asrs.org/content/images/cms/image_rib_macularhole_2_2858.jpg/image-full;size$250,194.ImageHandler)

33. [https://www.asrs.org/content/images/cms/image_rib_macularhole_2_2858.jpg/image-full;size\\$250,194.ImageHandler](https://www.asrs.org/content/images/cms/image_rib_macularhole_2_2858.jpg/image-full;size$250,194.ImageHandler)
34. <https://webeye.ophth.uiowa.edu/eyeforum/atlas/pages/extrafoveal-macular-hole/emh-1.jpg>

Fundus – RP

1. <https://imagebank.asrs.org/file/93471/retinitis-pigmentosa>
2. <https://educate.choroida.com/2021/07/05/retinitis-pigmentosa/>
3. <https://decisionmakerplus.net/dg-post/h35-52-retinitis-pigmentosa/>
4. <https://basicmedicalkey.com/retinitis-pigmentosa/>
5. <https://www.news-medical.net/health/What-is-Retinitis-Pigmentosa.aspx>
6. https://www.researchgate.net/figure/Fundus-photograph-of-an-individual-affected-with-retinitis-pigmentosa-The-fundus_fig3_40447070
7. <https://www.ncbi.nlm.nih.gov/books/NBK11553/figure/ch36clinicalerg.F15/>
8. https://www.brainkart.com/article/Retinal-Dystrophies--Retinitis-Pigmentosa_26087/
9. <https://entokey.com/retinitis-pigmentosa-and-allied-disorders/>
10. <https://entokey.com/retinitis-pigmentosa-and-allied-disorders/>
11. <https://retinography.org/sector-retinitis-pigmentosa/>
12. <https://retinography.org/sector-retinitis-pigmentosa/>
13. https://www.linkedin.com/posts/stevenlevymd_blindness-from-retinitis-pigmentosa-reversed-activity-7047214648877608960-ar4h
14. <https://atlas-1-elastic.atlasoph.com/photo.jsf;jsessionid=94EF0B6B067E676E8BCB3F2AD7B9885A?node=6475&locale=en>
15. <https://dizziness-and-balance.com/disorders/visual/retinopathy/RP.html>
16. <https://disorders.eyes.arizona.edu/disorders/retinitis-pigmentosa-ar>
17. <https://disorders.eyes.arizona.edu/disorders/retinitis-pigmentosa-ar>
18. <https://eyeandear.org/2020/07/a-new-era-in-retinal-research/>
19. <https://www.ncbi.nlm.nih.gov/books/NBK11553/figure/ch36clinicalerg.F14/>

20. https://commons.wikimedia.org/wiki/File:Fundus_of_patient_with_retinitis_pigmentosa,_end_stage.jpg
21. <https://healthjade.net/retinitis-pigmentosa/>
22. <https://www.reviewofoptometry.com/article/night-spots>
23. <https://www.visualsurgery.com/eye-conditions/retinal-diseases/other-retinal-diseases/retinitis-pigmentosa/>
24. https://www.researchgate.net/figure/Fundus-of-an-RP-patient-at-different-stages-a-Image-of-a-normal-healthy-eye-b_fig4_279155571
25. https://www.researchgate.net/figure/Fundus-of-an-RP-patient-at-different-stages-a-Image-of-a-normal-healthy-eye-b_fig4_279155571
26. https://www.researchgate.net/figure/Fundus-of-an-RP-patient-at-different-stages-a-Image-of-a-normal-healthy-eye-b_fig4_279155571
27. https://www.researchgate.net/figure/Fundus-of-an-RP-patient-at-different-stages-a-Image-of-a-normal-healthy-eye-b_fig4_279155571
28. <https://emedicine.medscape.com/article/1227488-overview?form=basic>
29. <https://www.centreforeyehealth.com.au/retinitis-pigmentosa-extract/>
30. <https://www.centreforeyehealth.com.au/retinitis-pigmentosa-extract/>
31. <https://www.centreforeyehealth.com.au/retinitis-pigmentosa-extract/>
32. <https://webvision.med.utah.edu/book/electrophysiology/the-electroretinogram-clinical-applications/>
33. <https://www.retinarevealed.com/retinitis-pigmentosa-page-34-of-49/>
34. <http://www.pjo.com.pk/30/2/12.CR%20Sana%20Nadeem%20Corrected.htm>
35. <http://www.pjo.com.pk/30/2/12.CR%20Sana%20Nadeem%20Corrected.htm>
36. <https://www.nyp.org/advances/article/ophthalmology/retinitis-pigmentosa-mitigating-retinal-degeneration-with-crispr-technology>
37. <https://www.ehu.eus/en/-/pacientes-con-retinosis-pigmentaria-en-la-pole>
38. https://en.wikipedia.org/wiki/Retinal_degeneration_%28rhodopsin_mutation%29
39. <https://imagebank.asrs.org/file/29807/x-linked-retinitis-pigmentosa>
40. <https://educate.choroida.com/2023/04/07/choroideremia-unveiling-what-you-need-to-know/>

41. <https://retinography.org/retinitis-pigmentosa-2/>
42. <https://retinography.org/retinitis-pigmentosa-2/>
43. <https://retinography.org/retinitis-pigmentosa/>
44. <https://retinography.org/retinitis-pigmentosa/>